analytical chemistry

pubs.acs.org/ac Article

Enhanced Laterally Resolved ToF-SIMS and AFM Imaging of the Electrically Conductive Structures in Cable Bacteria

Raghavendran Thiruvallur Eachambadi, Henricus T. S. Boschker, Alexis Franquet, Valentina Spampinato, Silvia Hidalgo-Martinez, Roland Valcke, Filip J. R. Meysman, and Jean V. Manca*

Cite This: *Anal. Chem.* 2021, 93, 7226−7234 Read Online

ACCESS | Metrics & More | Article Recommendations | Supporting Information

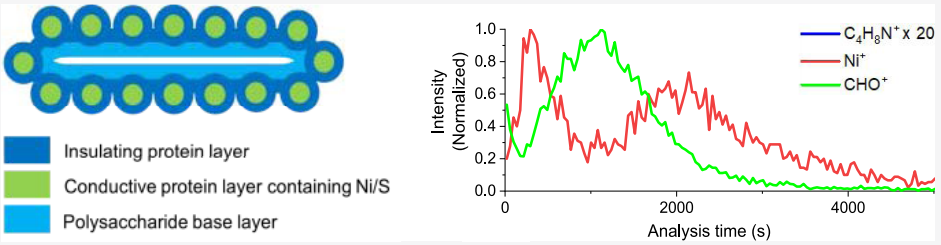

ABSTRACT: Cable bacteria are electroactive bacteria that form a long, linear chain of ridged cylindrical cells. These filamentous bacteria conduct centimeter-scale long-range electron transport through parallel, interconnected conductive pathways of which the detailed chemical and electrical properties are still unclear. Here, we combine time-of-flight secondary-ion mass spectrometry (ToF-SIMS) and atomic force microscopy (AFM) to investigate the structure and composition of this naturally occurring electrical network. The enhanced lateral resolution achieved allows differentiation between the cell body and the cell−cell junctions that contain a conspicuous cartwheel structure. Three ToF-SIMS modes were compared in the study of so-called fiber sheaths (i.e., the cell material that remains after the removal of cytoplasm and membranes, and which embeds the electrical network). Among these, fast imaging delayed extraction (FI-DE) was found to balance lateral and mass resolution, thus yielding the following multiple benefits in the study of structure−composition relations in cable bacteria: (i) it enables the separate study of the cell body and cell−cell junctions; (ii) by combining FI-DE with in situ AFM, the depth of Ni-containing protein—key in the electrical transport—is determined with greater precision; and (iii) this combination prevents contamination, which is possible when using an ex situ AFM. Our results imply that the interconnects in extracted fiber sheaths are either damaged during extraction, or that their composition is different from fibers, or both. From a more general analytical perspective, the proposed methodology of ToF-SIMS in the FI-DE mode combined with in situ AFM holds great promise for studying the chemical structure of other biological systems.

Cable bacteria are multicellular microorganisms that form long unbranched filaments and belong to the *Desulfobulbaceae* family.[1] They are the focus of interdisciplinary research due to their unique capability of conducting electrical currents over centimeter distances,[2,3] a process also known as long-distance electron transport (LDET). Cable bacteria have been found to thrive in different environments such as fresh water[4,5] and marine sediments,[6,7] and have also been found in different parts of the world.[7] Cable bacteria display a distinct morphology with parallel ridges running along the length of the filament.[1,8,9] Scanning electron microscopy of the cross section of a cable bacteria revealed the presence of fibers of about 50 nm in diameter under the ridges and a cartwheel structure at the junctions.[8] These fibers are embedded in the periplasm (i.e., in space between the cytoplasmic membrane and the bacterial outer membrane) and were suspected to be the conductive structures[8] (Figure 1A−C).

Recently, Meysman et al. experimentally investigated the conductivity of these fibers.[9] A sequential extraction procedure was developed[8] (see the Experimental Section) from which the fiber structures can be isolated from the cable bacterium filaments.[8] After chemical removal of cytoplasm and membranes, a so-called fiber sheath remains, which embeds the periplasmic fibers.[9−11] The fiber sheath flattens when air-dried (Figure 1D), and the top part of this fiber sheath mirrors the bottom part due to its cylindrical symmetry.[8]

Meysman et al. demonstrated that fiber sheaths were indeed highly conductive.[9] Fiber sheaths were placed on top of two gold pads with a nonconductive oxide spacing, and when applying a potential difference between the two pads, a flow of current indicated that the periplasmic fibers are the conductive conduits. These results were subsequently confirmed by

Received: January 21, 2021
Accepted: April 19, 2021
Published: May 3, 2021

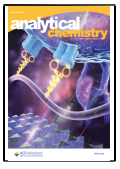

https://doi.org/10.1021/acs.analchem.1c00298
Anal. Chem. 2021, 93, 7226−7234

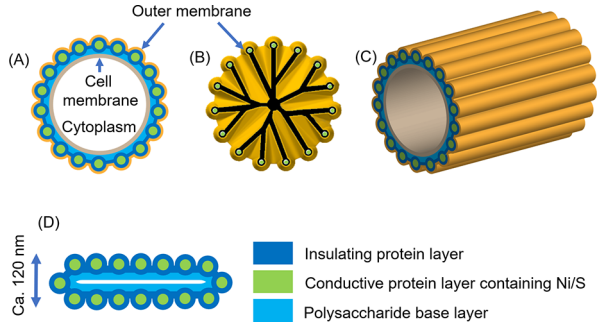

Figure 1. Schematic of a cable bacterium. Cross section of a cable bacterium filament at the center of a cell (A) and at the junction (B) showing the cartwheel structure. Three-dimensional (3D) representation of the ridged cell is shown in (C). After the sequential extraction procedure, a flat ca. 120 nm thick fiber sheath is obtained, seen in (D). The spokes of the cartwheel are shown in black as its composition is unknown (adapted from Cornelissen et al.[8] and Boschker et al.[11])

conductive atomic force microscopy (C-AFM).[10] The conductivity of these periplasmic fibers (>20 S/cm) not only rivals that of doped organic semiconductors,[9] but the length scale of electron transport is also more than 3 orders of magnitude longer than previously known for microbial structures.[3] Therefore, there is a strong interest in this material for future biodegradable electronic applications.

To better understand the unique electrical properties of cable bacteria, a key challenge is to unravel the composition of the electrically conductive fibers. Here, we combine time-of-flight secondary-ion mass spectrometry (ToF-SIMS) and AFM to investigate the structure and composition of this naturally occurring electrical network of fibers with enhanced lateral resolution. Mass spectrometry-based chemical imaging is widely used for different types of cellular analyses.[12−14] Various SIMS techniques are available, of which ToF-SIMS and nanoscale secondary-ion mass spectrometry (NanoSIMS) are routinely utilized. Of the two, NanoSIMS provides the best lateral resolution (<50 nm) but is limited in the number of elemental masses that can be simultaneously detected.[15−19] With isotopic labeling, NanoSIMS can be used to localize the incorporation of different elements (C, N, S) within the cell compartments,[20−22] and this technique has also been recently applied to cable bacteria to investigate the relation between LDET metabolism and filament growth.[20−22]

ToF-SIMS uses a polyatomic or gas cluster ion source in addition to monoatomic sources, and, as such, it is less destructive as compared to NanoSIMS. The Bi_3^+ ion source was found to be both surface-sensitive as well as providing the best imaging contrast.[23] Large molecular fragments up to 1000 Da can be analyzed and with a typical lateral resolution of 100 nm to 10 μm.[24] Generally, two different modes are employed in ToF-SIMS.[25] The first one is the high current bunched (HCB) mode, also referred to as mass-spectrometry mode, which targets high mass resolution but has a restricted 2−10 μm lateral resolution.[25,26] Mass resolution can be defined as the ability to distinguish two peaks of slightly different mass-to-charge ratios ($m/\Delta m$) in a mass spectrum. The HCB mode uses three electrostatic lenses and a primary ion buncher system, ensuring short pulses of less than 1 ns; such short pulse duration results in a typically high mass resolution $m/\Delta m$ > 10 000. The second ToF-SIMS mode is the burst alignment mode or the fast-imaging (FI) mode, where a high lateral resolution of about 400 nm is obtained but with a loss of mass resolution.[27] A narrow beam is used in the FI mode, with a beam diameter well below 1 μm using two electrostatic lenses. The time width of the primary ion pulse is on the order of tens of nanoseconds, leading to a low unit mass resolution ($m/\Delta m$ ∼ 200).[25−27] The mass resolution can be improved by maintaining the lateral resolution of the FI mode using delayed extraction. This third ToF-SIMS mode is termed as fast imaging delayed extraction (FI-DE). In delayed extraction, ion extraction is decoupled from ion generation by switching off the extraction voltage for several nanoseconds after firing the primary ion pulse. A plume of ions is obtained just over the surface, a field-free emission of secondary particles. Due to this decoupling, the long primary ion pulse required to obtain a high lateral resolution does not affect the mass resolution.[25,27] The plume moves away from the surface before the extraction voltage is switched on because of which the topographic effects are reduced, the number of secondary ions collected is increased, and sharper lateral images with a better signal are obtained. Quite recently, Benettoni et al. were able to obtain a high lateral resolution of ∼100 nm on a chessboard sample, with a mass resolution on the order of 5000. However, the lateral resolution was reduced to 222 nm on an algal biofilm.[28]

Recently, TOF-SIMS analysis combined with in situ AFM has generated the first insights into the conductive network of the cable bacteria[11] (see Figure 1D for a schematic representation of the results). To this end, ToF-SIMS HCB analysis using Bi_3^+ was combined with interlaced argon cluster sputtering and applied to fiber sheaths. This provided high-resolution depth profiles of both organic and inorganic constituents at a low lateral resolution.[11] High surface counts were recorded for amino acid fragments, including aromatic amino acids in both positive and negative modes. Nickel and sulfur signals showed subsurface peaks in the positive and negative mode, suggesting that the fiber's central core is protein-rich with Ni and S. After 150 s of sputtering, signals from the oxygen-rich fragments, including carbohydrate-specific ions peaked while the signals from nitrogen-containing fragments leveled off. By combining the results from other complementary characterization techniques, a structural model of the fiber sheath was made (Figure 1D): fibers are made of protein, lying on top of a polysaccharide-rich base layer, most likely consisting of peptidoglycan. The fiber itself is made of a Ni-rich protein core surrounded by a thin layer of Ni-deficient protein, which is termed as a fiber core/shell structure.[11] Although the HCB mode was instrumental in identifying various fragments with a high mass resolution, it comes with a sacrifice of lateral resolution that does not allow to separately study the composition of the fibers and the cartwheel structure at the junctions.[11] To provide more details on the conductive fibers present in the fiber sheath, we employed and compared the three mentioned ToF-SIMS modes. The FI-DE mode, which balances the lateral and mass resolution, in combination with in situ AFM, is expected to offer the unique benefit of a direct and more detailed depth calibration.

EXPERIMENTAL SECTION

Sample Preparation. Sediments containing cable bacteria were collected from a salt marsh creek bed. These sediments were sieved, homogenized, repacked in PVC core liner tubes (diameter: 40 mm), and were subsequently placed in aerated, artificial seawater. These incubations are known to consistently develop thick, ca. 4 μm diameter, cable bacterium filaments,

https://doi.org/10.1021/acs.analchem.1c00298
Anal. Chem. 2021, 93, 7226−7234

which facilitates their isolation from the sediment and fiber sheath extraction.

To collect the cable bacterium filaments and extract the fiber sheaths, a small amount of sediment was placed on a microscope coverslip. Multiple droplets (20 μL) of Milli-Q water were placed near the sediments. Under a stereomicroscope, filaments were picked from the sediments using custom-made glass hooks made from Pasteur pipets. Filaments were cleaned and washed at least six times by transferring them between droplets. The cleaned intact filaments were subsequently incubated in a 20 μL droplet of sodium dodecyl sulfate (SDS) for 10 min, followed by six MilliQ droplet washes. Filaments were further subjected to a 10 min incubation in a 20 μL of 1 mM sodium ethylenediaminetetraacetate (EDTA) solution, again followed by six washes in Milli-Q.[8] The extracted material represents the fiber sheath containing the conductive fibers.

Fiber sheaths were deposited as clumps on a 1 cm × 1 cm diced Au-covered Si wafer for ToF-SIMS analysis. Samples were first imaged in an optical microscope to identify areas to be analyzed. Three samples prepared on different occasions were analyzed under HCB and FI-DE modes, and five areas from two clumps of fiber sheaths prepared during the same run were analyzed under combined ToF-SIMS/AFM modes.

For conductive AFM, one filament was deposited on a 1 cm × 1 cm diced SiO_2-covered Si wafer (Figure S6). This wafer was then affixed onto a steel disc using silver paste (EM-Tec AG44 conductive silver paint). The detailed procedure can be found elsewhere.[10] Four replicates were analyzed using C-AFM.

ToF-SIMS Analysis. ToF-SIMS analysis was performed using TOF-SIMS NCS (IONTOF GmBH, Germany) located at imec, Leuven (Belgium). In the HCB mode, ToF-SIMS was carried out in an interlaced mode using a Bi_3^+ analysis beam (30 keV, current ~0.35 pA, 100 × 100 μm^2 area, 256 × 256 pixels) and an Ar_{4000}^+ gas cluster ion beam (Ar GCIB, 10 keV, current 1 nA, 400 × 400 μm^2 area). Fast imaging (FI) was done by fine-tuning the existing factory settings (Bi_3^+, 30 keV, ~0.12 pA, 30 × 30 μm^2, 512 × 512 pixels). Only surface scans were obtained in the case of FI mode. For FI-DE, the existing setting for fast imaging was initially set with Bi_3^+ ions (30 keV, current ~0.15 pA, 30 × 30 μm^2 area). The parameters for delayed extraction were optimized, namely, delay time, the analyzer lens voltage, X/Y analyzer deflection plates, and surface and virtual drift potentials (VDPs)[27]. A delayed extraction of 85 ns was found to be appropriate. A cycle time of 50 μs was used. In both cases, filaments were not necessarily sputtered until only the substrate remained, as shown in Figure 4.

SurfaceLab software (v7, IONTOF, Germany) was used for data analysis. In the HCB mode, mass spectra were internally calibrated using $C_2H_3^+$, $C_3H_4^+$, $C_3H_5^+$, $C_4H_5^+$, and Au^+. Mass peaks were identified based on the earlier ToF-SIMS work with cable bacteria.[11] In the FI-DE mode, mass spectra were internally calibrated using $C_2H_3^+$, $C_3H_4^+$, $C_3H_5^+$, and $C_4H_5^+$. When necessary, lateral shift correction was done using the Shift correction subprogram of the Images program. Regions of interest (ROIs) were created to analyze cell bodies and junctions separately (Figure 4). The peak list obtained from the HCB mode was truncated to remove nonresolvable signals. Identified peaks from both the HCB and FI-DE modes are provided in Tables S2−S6.

Principal component analysis (PCA) was performed using OriginLab Pro v2020's principal component analysis app. Three replicates of profiles of various fragments from HCB and FI-DE modes were separately analyzed after mass calibration with the same peak lists. The peak width of each signal was adjusted by overlapping the three spectra and fixing the peak width. Depth (or analysis time) profiles of selected peaks were imported into OriginLab Pro software, in which the profiles of individual fragments were normalized to their maximum value. Profile data of the various masses until the maxima of the oxygen-containing organic ions were used for PCA, identical to those of Boschker et al.[11] Fragments used in PCA are indicated in Tables S2−S6.

Combined ToF-SIMS/AFM Analysis. In situ AFM was used in the contact mode to analyze the depth at which the Ni signal maximum was found and to estimate the midpoint of the carbohydrate layer. PPP-EFM probes (NanoWorld AG) with a nominal spring constant of 3 N/m were used in the contact mode. The AFM probe and the area to analyze were first aligned using a test area close to the area of interest. After a scan of a known area was obtained using ToF-SIMS, the coordinates were noted down using Surfacelab software. Then, the sample was driven to the AFM part of the instrument. The area of interest was retrieved in the AFM by trial and error, and the coordinates of this area were noted down using Surfacelab software. The software calculates the lateral vector shift based on the two coordinates.

A 10 × 20 μm^2 AFM image of the area to be sputtered was captured with a pixel size of about 78 nm. An enlarged area of about 15 × 30 μm^2 was sputtered by Bi_{3+} ions with the conditions mentioned earlier. Sputtering was paused before and after the peak in the Ni^+ ion signal emerged. During the pause, the stage was moved within the same hybrid ToF-SIMS/AFM instrumental setup—without exposure to the lab atmosphere and therefore no contamination—to the in situ AFM location. AFM imaging was taken from the sputtered area. These two images were leveled by mean plane subtraction, aligned using the "mutual crop" module of *Gwyddion* software, and then the second image was subtracted from the first. In this difference image, the amount of material removed from the cell body can be determined. Another AFM image was taken at a point in the carbohydrate region.

Conductive AFM. AFM analysis was performed on a Multimode 8 (Bruker, Santa Clara, CA) with a Nanoscope V controller located at UHasselt. A CDT-NCLR probe with a nominal spring constant of 72 N/m was used. A fiber sheath was placed on a silicon substrate with a 100 nm thick SiO_2 layer acting as an insulator. This substrate was then connected to a steel disc using silver paste (Figure S6). One end of the fiber sheath was electrically connected to the substrate holder, while the other end of the filament was left free. Bias is applied to the sample via the sample holder, and the conductive probe is electrically connected to the TUNA application module, which contains a current amplifier. This application module is, in turn, connected to the AFM controller. Current can only flow if there is an electrical connection between the substrate holder and the AFM probe, thereby completing the electrical circuit. Measurement was initially carried out in Scanasyst mode to obtain topography. After an area of interest was localized, AFM was switched to the C-AFM mode, which works in a contact mode.

Due to the high spring constant of the cantilever, specific areas from a cell were relatively easily removed by scratching a

https://doi.org/10.1021/acs.analchem.1c00298
Anal. Chem. 2021, 93, 7226−7234

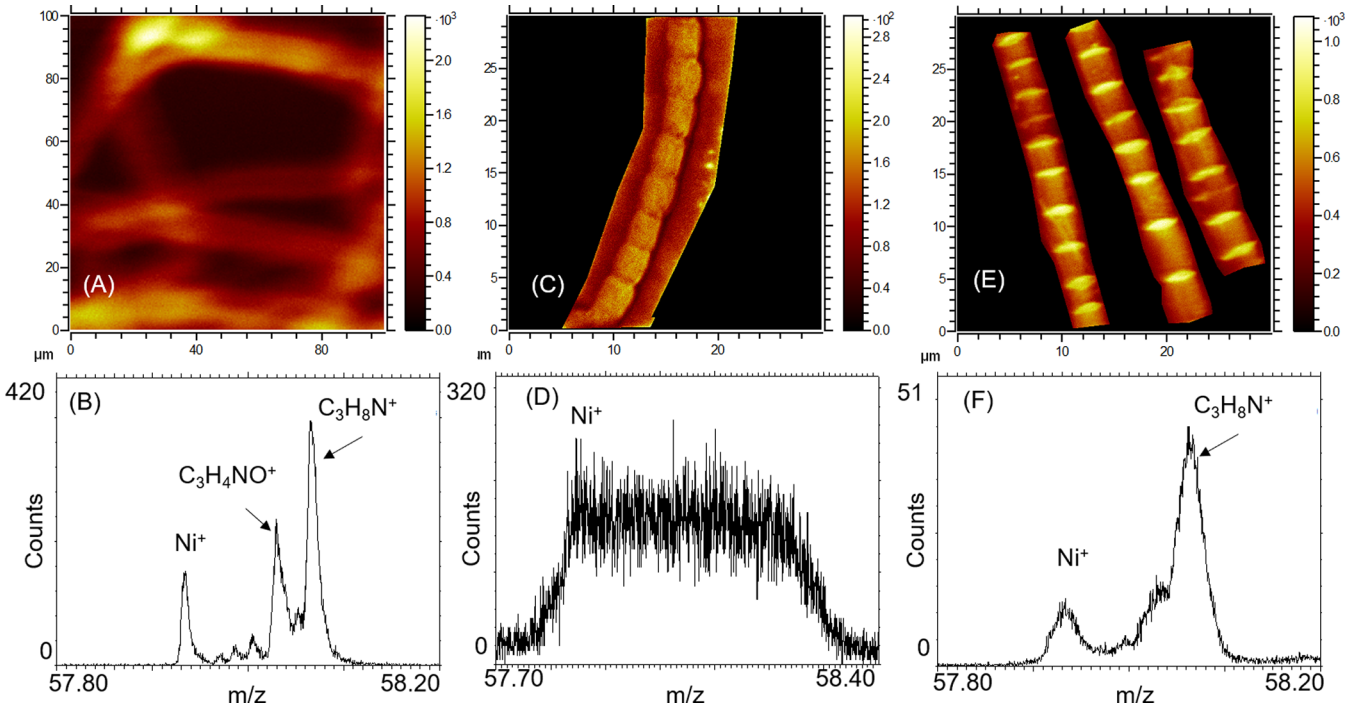

Figure 2. Study of ToF-SIMS imaging modes on the lateral and mass resolution: HCB (A, B), FI-DE (C, D), and FI modes (E and F). (A)−(C) are the total intensity images. The lateral resolution of FI-DE (E) and FI (C) is better than HCB (A). On the other hand, the mass resolution ($m/\Delta m$) of Ni^+ of the HCB mode (B) was 7000, whereas in the FI-DE mode (D) it was lower at 2100, sufficient to resolve the Ni^+ signal. Mass resolution in the FI mode is insufficient to resolve Ni^+.

given area continuously in the contact mode with a high force (15 μN) to disrupt more than half of the electrical connections within a cell. This creates a trench that goes all the way to the substrate. However, a much lower force (2.2 μN) was applied to gently scrape bacteria's surface to visualize the electrical pathways, identical to our earlier work.[10]

RESULTS AND DISCUSSION

Comparison of Lateral Imaging and Mass Resolution. To qualitatively appreciate the mass resolution and quantitatively measure mass resolution, fiber sheaths were imaged using three different ToF-SIMS modes. Figure 2 shows the cable bacterium filaments from a single sample preparation imaged in HCB (A and B), FI (C and D), and FI-DE (E and F) modes. This illustrates the capabilities of these modes in terms of lateral imaging resolution (upper panels: A, C, and E) and mass resolution of ionized fragments (bottom panels: B, D, and F).

The HCB mode provides a high mass resolution spectrum (Figure 2A,B, S1). A high mass resolution of Ni^+ (m/z = 57.93) of 7000 was measured. Figure 2A clearly shows the poor lateral imaging resolution, in which the filaments appear fuzzy and much thicker than their nominal width of 4−5 μm. Using FI mode, a substantial improvement in the lateral imaging resolution was obtained, with the cell junctions being resolved from the cell bodies (Figure 2C). However, the mass resolution was at best on the order of a few hundred. For instance, the Ni^+ signal was not resolved because of the low mass resolution (131); it also encompassed signals from $C_2H_4NO^+$ (m/z = 58.029) and $C_3H_8N^+$ (m/z = 58.065) (Figure 2C,D). This lack of mass resolution is insufficient for biological analysis.

In the FI-DE mode, a lateral resolution was sufficient to separate cell junctions from cell areas (Figure 2E), and the mass resolution of Ni^+ was 2100 (Figure 2F). Complete spectra obtained from FI-DE can be seen in Figure S1. Although the mass resolution does not match up to HCB, it was sufficient to resolve the Ni^+ signal. FI-DE improved the lateral resolution, where the cell junctions and bodies are resolved. The mass resolution was found to be sufficient to resolve Ni and fragments of amino acids, polysaccharides, and others (see Tables S2−S6).

Comparison of Depth Resolution. We compared the depth resolution between HCB and FI-DE. HCB uses a dual-beam, where argon GCIB is used to sputter away the analyzed area. However, FI-DE is a single-beam measurement, where the Bi_3^+ beam is also responsible for sputtering. Here, we show that FI-DE has a better depth resolution compared to HCB.

Figure S2 shows the normalized three main trends in the sputtering-time depth profiles as found in the HCB mode, based on the study by Boschker et al.[11] The first one or two data points are usually related to surface transients, i.e., C- or N-based ions derived from contamination (this surficial zone extends until the local minimum of CHO^+ signal). Below this, the first signal observed is of high levels of nitrogen-containing fragments such as $C_4H_8N^+$, a fragment of proline, and an amino acid used in the synthesis of proteins, which stands for the profile of all amino acid fragments. Ni and its isotopes show a subsequent peak, and a third and broader peak is displayed by oxygen-containing fragments such as CHO^+, most likely derived from carbohydrates in the peptidoglycan layer. $C_4H_8N^+$ shows a very high surface signal, indicating the presence of a protein layer at the surface. The subsurface peak in Ni has been linked to a Ni-containing protein that likely plays a role in the electron transport within the conductive

https://doi.org/10.1021/acs.analchem.1c00298
Anal. Chem. 2021, 93, 7226−7234

fibers.[11] As the intensity of Ni^+ decreases, oxygen-containing fragments such as CHO^+ become higher in intensity. A second Ni peak is seen at about 164 s of sputtering time. Although not entirely resolved, this second peak is likely due to the Ni-protein layer in the bottom part of the fiber sheath, which is essentially a mirrored duplicate of the part of the sheath away from the substrate.

Principal component analysis (PCA) of selected peaks (Figure S3A,C) showed clustering of oxygen-containing fragments and nitrogen-containing fragments with Ni. Boschker et al. proposed that the fiber sheath is made of a thin protein layer containing Ni-containing proteins and a polysaccharide-rich layer present under the protein layer.[11] However, in many cases, depth smearing occurs possibly due to a different structure (cell bodies vs junction). When cells retain an amount of cytoplasm after incomplete extraction, only the first subsurface Ni peak can be detected.[11] So, an additional benefit of FI-DE as employed here is that it also enables the imaging of the bottom part of the fiber sheath.

A significant improvement made with FI-DE is that regions of interest (ROIs) can be separately defined for the cell body and the cell junction (Figure 3A–C). The signals from the body of cable bacteria can be studied separately from the cell junctions, which reduces depth smearing, as junctions are thicker than the rest of the filament.[8] Cell junctions can be distinguished from the rest of the bacteria with FI-DE by the total counts measured at the junction, possibly due to the higher material yield. Cell junctions contain more material than the cell body, which implies more counts from this region (Figure 3A). The newly forming division planes, which are rings consisting of protein FtsZ,[29] were not considered in the junction analysis since it is not known whether their structure is similar to that of an established division plane. Depth resolution was further improved in FI-DE imaging since more data points were obtained for a given thickness of material sputtered, thanks to a single beam. The first seven data points, corresponding to the local minimum in the CHO^+ signal, are again related to the surface transient, i.e., organic contamination on the surface.

The filament signals in the FI-DE mode consistently revealed a sharp subsurface Ni peak and a distinctive second peak (Figure 3D). $C_4H_8N^+$ has an intense surface signal seen earlier in the HCB mode and a secondary peak just before the Ni signal reaches a peak, which was not seen in the HCB mode. The carbohydrate oxygen-containing fragment CHO^+ is prominently present between the two peaks of Ni^+ signals and nitrogen-containing signals. The second peak of the Ni signal and the peak of the $C_4H_8N^+$ signal confirm that Ni is found in the protein, and the basal sheath is held together by a carbohydrate-containing layer. The second Ni^+ peak and the $C_4H_8N^+$ peak from the cell bodies (Figure 3E) were sharper than the signals from the filaments. This is because junctions are thicker and possibly have a different composition due to the presence of the cartwheel structure. The PCA analysis of the various identified fragments from cell bodies (Figure S3B,D) showed a clustering of the nitrogen-containing fragments and the oxygen-containing fragments, similar to that seen in the HCB mode.

Combined ToF-SIMS/AFM Study of Fiber Sheaths. Depth profiles in ToF-SIMS provide the intensity of various fragments as a function of time. By using in situ AFM at appropriate intervals, analysis time can be translated in terms of distance. The depth patterns of various fragments as

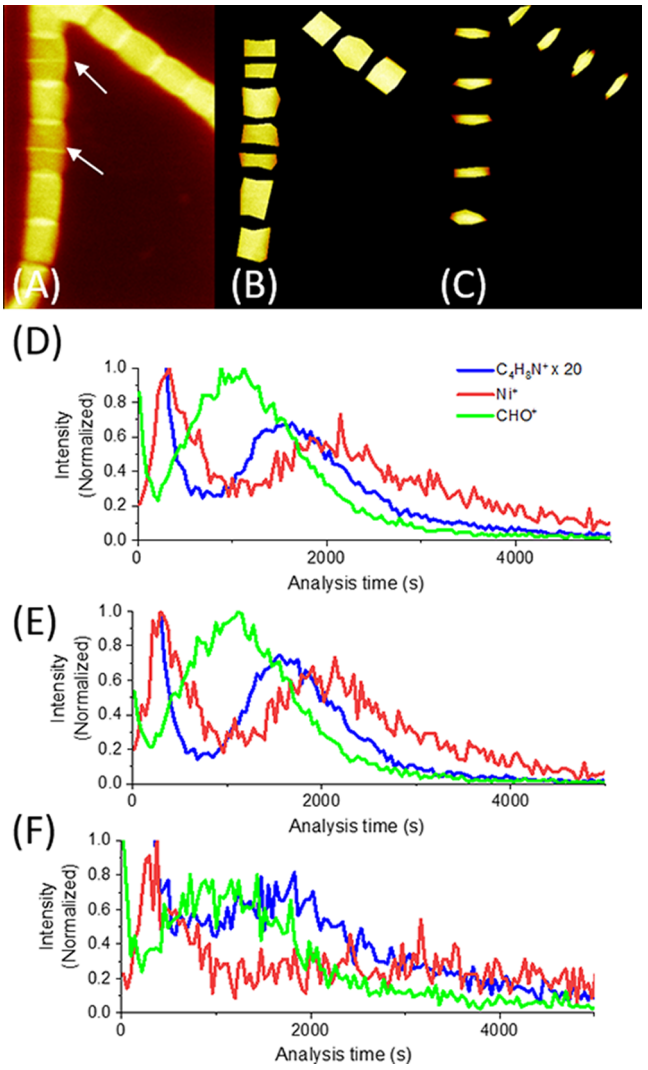

Figure 3. (A) Lateral total intensity image of two cable bacteria filaments, with two white arrows showing the newly forming cell junctions. The enhanced lateral resolution with FI-DE enabled the study of signals from various fragments from the body (B) and the junctions (C) separately. Trends of $C_4H_8N^+$, Ni^+, and CHO^+ signals, normalized to their highest intensity, from the filaments (D), cell bodies (E), and cell junctions (F). The $C_4H_8N^+$ signal was magnified 20× to show the second peak in the profile.

obtained by combining AFM and the HCB mode were previously shown by Boschker et al.[11] Here, we combine AFM with the FI-DE mode. Figure 4 describes how the distance of the Ni^+ signal from the top surface is measured. Figure 4A is the height image before analysis commenced. The change in the normalized intensity of the sum of two Ni isotopes, $^{58}Ni^+$ and $^{60}Ni^+$, and CHO^+ signals during sputtering are given as a function of data points (Figure 4F). One data point corresponds to one scan by the Bi_{3+} ions of the given area. Profiles of $^{58}Ni^+$, $^{60}Ni^+$, and CHO^+ fragments in Figure 4F were obtained from the dotted blue polygons in Figure 4D. As the combined Ni signal was higher in intensity, the analysis was paused at datapoint 6, and another AFM image was taken (Figure 4B).

Subtracting the image in Figure 4B from that in Figure 4A gave a difference image shown in Figure 4C. The sputtered depth was measured by averaging the area within the dotted blue polygons of Figure 4C and subtracting from the

https://doi.org/10.1021/acs.analchem.1c00298
Anal. Chem. 2021, 93, 7226−7234

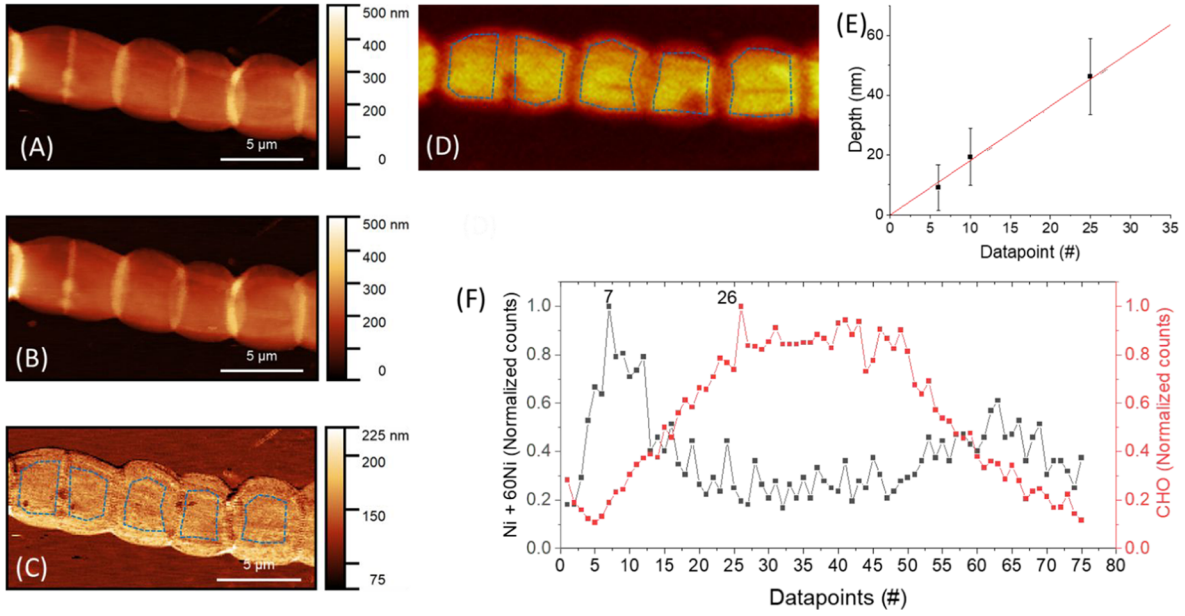

Figure 4. Combined ToF-SIMS/AFM analysis of a fiber sheath filament. An AFM image was captured (A) before sputtering and (B) after sputtering until datapoint 6. The total intensity ToF-SIMS image is shown in (D). (B) and (A) were aligned, and (B) was subtracted from (A), resulting in a difference image (C). The removed thickness was calculated by subtracting the substrate's mean height from the mean height of the bacteria body (dotted blue polygons), plotted in (E). (F) The change in Ni^+ and CHO^+ counts (normalized, obtained from cell bodies, marked as dotted blue polygons in D) as a function of captured data points. Ni^+ peak is seen at datapoint 7, and CHO^+ signal reaches a maximum at datapoint 26. The second Ni peak is seen at datapoint 64.

substrate's height. This corresponds to 9.1 ± 7.7 nm. Another AFM image was taken at data point 10 after the peak of the Ni^+ signal was crossed. A third AFM image was taken at datapoint 25 in the carbohydrate-rich region. After measuring the sputtered depths for data points 10 and 25, a line fit was made. The initial condition was that no material is removed before the commencement of analysis (i.e., y (x = 0) = 0 nm). The peak of the Ni^+ signal was seen at datapoint 7, corresponding to 12.7 nm. Based on an average of five replicates, an average depth of 11.8 ± 0.6 nm was measured for the Ni maximum, slightly lower than the previously reported value of 15 ± 3 nm.[11] However, the midpoint of the flat region of the oxygen-containing organics varied between samples (between 32 and 68 nm, see Table S1). This is probably because different filaments contain varied amounts of cytoplasm, although undergoing the same extraction procedure.

By combining in situ AFM measurements with ToF-SIMS, we measured the depth of Ni^+ without having to remove the sample out of a vacuum. This is of importance to materials that are sensitive to exposure to the atmosphere. Also, keeping the sample within the equipment ensures the same instrument parameters such as vacuum and analysis beam conditions before and after AFM measurements. The lateral resolution obtained by FI-DE ensured a good correlation between SIMS and AFM data, and a more accurate determination of the depth at which Ni signals reached a peak in its counts.

Composition of the Cell Junctions. Cell junctions contain the interconnecting structures that provide cable bacteria filaments with a redundant fail-safe electrical network.[10] The cartwheel structure present at the junctions is suspected of containing the interconnecting structure, although there is no direct proof available.[8,10] Interestingly, junctions in fiber sheaths appear flatter compared to intact filaments.[8] Thanks to the lateral resolution offered by FI-DE, we can isolate signals from the junctions. Due to the improved depth resolution, we were able to study the various profiles' trends as a function of depth.

The profiles of the various fragments from the junctions showed similar trends (Figure 3F). The Ni signal showed a subsurface peak, which comes from the conductive fibers that run parallel along with the cells and across the junction (Figures 3F and S4B). The amino acid peak is not as pronounced as that seen in the cell body. It appears that there are relatively more amino acid fragments between the two sheaths at the junction as compared to the cell body (Figure S4A). Also, the rate of the decreased intensity of the second amino acid peak from the cell junctions is lower. A look at the total number of signals of the various identified protein and carbohydrate fragments, normalized to the total counts of identified fragments, indicates that the ratio of Ni to protein fragments at the junction is lower than that of the body (Figure S5). The relative amount of Ni present in the junction is identical to that of the body, suggesting that Ni is absent within the junction. Hence, the junction's interconnects are either damaged, its composition is different from the fibers, or both. However, the LEXRF analysis of the fiber sheath[11] indicates a higher amount of Ni in certain sections of the sheath. Additional studies are required, such as analysis of cross sections, to arrive at a definite conclusion.

A conductive AFM experiment was carried out on a fiber sheath by intentionally disrupting the conductive pathways identical to those performed on untreated intact filaments[10] (Figure S6) to check whether the electrical interconnections seen in the latter are present in the former. The antiparallel cuts in the filaments can be seen as trenches in the height image, also marked by green arrows (Figure 5). Carbon paste, connected to the fiber sheath away from the top-left corner (not seen), acts as an electrode. The AFM probe acts as the second electrode. A pixel will appear bright in the AFM current

https://doi.org/10.1021/acs.analchem.1c00298
Anal. Chem. 2021, 93, 7226−7234

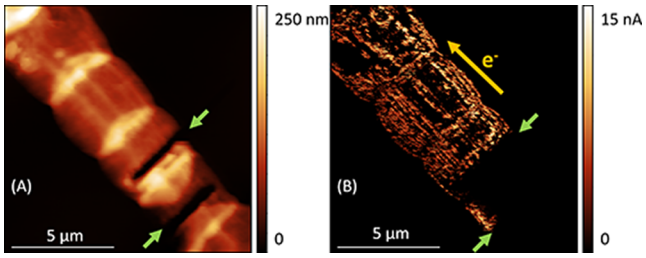

Figure 5. Conductive AFM images. (A) Topography map and (B) current map of a fiber sheath with two antiparallel cuts across its width (green arrows). The fiber sheath is biased using carbon paste on the top-left corner (not seen). As the probe scans the surface from the bottom, structures electrically connected between the area under the AFM probe and the carbon paste appear bright, i.e., conductive, seen in (B). The direction of the current flow is given by the orange arrow in (B).

image (Figure 5B) if the AFM probe that is positioned on the fiber sheath at that pixel is electrically connected to both the electrodes. Conductive areas can be seen from the top-left until the first cut. Some areas that still remain electrically connected to the carbon paste can be seen between the first cut and the second, along the left edge. The rest of the area remains nonconductive, as they are not electrically connected to the carbon paste. This shows that the junction in the extracted fiber sheaths does not provide electrical interconnection of fibers, as seen in untreated filaments.[10] As already hypothesized from the FI-DE experiments, C-AFM measurements suggest that interconnects within the junction of extracted fiber sheaths are either damaged, or its composition is different from the fibers, or both. Further research is needed to resolve this issue and elucidate the cartwheel structure's nature in the junction of cable bacteria.

CONCLUSIONS

We investigated the structure and composition of cable bacteria with an enhanced lateral resolution, allowing differentiation between the cell body and the structured cartwheel junctions. The combination of ToF-SIMS FI-DE and in situ AFM proved to be a powerful approach for this. Three ToF-SIMS modes were compared, viz., high current bunched (HCB), fast imaging (FI), and fast imaging delayed extraction (FI-DE). The HCB mode provided the best mass resolution but lacked lateral resolution. On the other hand, the FI mode provided a high lateral resolution but lacked mass resolution, which at best was in the order of a few hundreds. However, we found that FI-DE provides a good balance between the mass and lateral imaging resolution. Not only a submicron resolution was obtained, but we observed the mass resolution to be sufficient to resolve signals from Ni and other protein and carbohydrate-related fragments. To avoid depth smearing, we used ROIs to analyze the bodies and junctions of the filaments separately, thanks to an improved lateral resolution. Ni signals reached a subsurface peak, followed by a decrease, and then reached a second maximum. The secondary Ni peak was not seen earlier with HCB analysis.

The maximum intensity of the CHO^+ signal was found between the two Ni maxima, indicating a carbohydrate-rich material. Furthermore, we also observed enhanced depth resolution by following the depth profile of the $C_4H_8N^+$ signal, in which we observed a seconday peak just before the second maxima of the Ni^+ signal. This confirms the earlier result that Ni is present in the still unidentified protein. By using an advantageous combination of ToF-SIMS and AFM, we were able to carry out both SIMS and AFM imaging in an ultrahigh vacuum, avoiding contamination by bringing the sample to atmospheric conditions for external AFM imaging. Not only finding the sputtered location in an external AFM would have been difficult and time-consuming, but also to analyze the same area back in SIMS with the right orientation would be daunting. We were able to determine the depth of subsurface maxima of the Ni^+ signal and the various depths at which carbohydrate signals were found. Comparing Ni to protein ratio in the body and junction of bacteria indicated a higher ratio in the body than at the junction. Also, the relative counts of Ni in the body were equal to that of the junctions, indicating the absence of Ni within the junction. This absence could be attributed to the differences in the composition of the junction and the body, or the interconnecting structure between adjacent cells seen in intact filaments is damaged during the extraction procedure or both. C-AFM measurements show that the interconnections at the junction seen earlier in intact filaments are not present in the fiber sheath. Not much is yet known about the composition and properties of the cartwheel structure in intact filaments. The cross sections of intact filaments and fiber sheaths obtained by cryo-microtome and the study of these cross sections using ToF-SIMS and other complementary techniques such as C-AFM could give better insight into the composition of the cell−cell junction. Furthermore, the continued use of the proposed ToF-SIMS/SPM measurement methodology together with complementary analytical and electrical techniques could be powerful toward a better understanding of the underlying electrical transport properties in cable bacteria and, in particular, to clarify the role of Ni and S. This teaming up with complementary techniques is essential since ToF-SIMS can provide insights into the chemical composition of cable bacteria but is not a quantitative technique and therefore does not allow to quantify the Ni and S density. In our recent work on the intrinsic electrical properties of cable bacteria, we have observed an Arrhenius-type relation for the temperature dependence of the electrical conductivity and electron mobility over a broad temperature range (−195 to +50 °C), demonstrating that charge transport is thermally activated.[30]

From a more general analytical perspective, the proposed methodology of ToF-SIMS in the FI-DE-mode, combined with AFM, could also be beneficial in resolving the structure and composition of other biological systems. An in situ AFM can be used to measure the depth of various features of interest. However, AFM is foremost an imaging (microscopy) tool. Hence, AFM can also be used to identify the area of interest. For example, when micron-sized cells are dispersed over a substrate, it is impossible to see them using the in-built camera of the ToF-SIMS equipment. The in situ AFM can be used to image areas to identify the location of these cells in a given area in the substrate before they are analyzed using SIMS, thus saving time.

ASSOCIATED CONTENT

Supporting Information

The Supporting Information is available free of charge at https://pubs.acs.org/doi/10.1021/acs.analchem.1c00298.

HCB and FI-DE ToF-SIMS spectra of the fiber sheath; trends of various fragments as a function of the

https://doi.org/10.1021/acs.analchem.1c00298
Anal. Chem. 2021, 93, 7226−7234

sputtering time; PCA analysis of the fiber sheath spectra in HCB and FI-DE modes; comparsion of three typical trends in the body and at the junction; comparison of various fragments normalized to total intensity of identified fragments; schematic of C-AFM setup; depth measurements of Ni^+ and CHO^+ signals; and lists of identified fragments associated with the protein layer, Ni, polysaccharide layer, other general fiber sheath fragments, and fragments derived from medium, wafer, and the sediment matrix (PDF)

AUTHOR INFORMATION

Corresponding Author

Jean V. Manca − *UHasselt—X-LAB, 3590 Diepenbeek, Belgium*; Email: jean.manca@uhasselt.be

Authors

Raghavendran Thiruvallur Eachambadi − *UHasselt—X-LAB, 3590 Diepenbeek, Belgium*; orcid.org/0000-0002-2460-8577

Henricus T. S. Boschker − *Department of Biotechnology, Delft University of Technology, 2629 HZ Delft, The Netherlands; Department of Biology, University of Antwerp, 2610 Wilrijk, Belgium*

Alexis Franquet − *Materials and Components Analysis − Compositional Analysis, Imec vzw, 3001 Leuven, Belgium*

Valentina Spampinato − *Materials and Components Analysis − Compositional Analysis, Imec vzw, 3001 Leuven, Belgium*; orcid.org/0000-0003-3225-6740

Silvia Hidalgo-Martinez − *Department of Biology, University of Antwerp, 2610 Wilrijk, Belgium*

Roland Valcke − *UHasselt—Molecular and Physical Plant Physiology, 3590 Diepenbeek, Belgium*

Filip J. R. Meysman − *Department of Biotechnology, Delft University of Technology, 2629 HZ Delft, The Netherlands; Department of Biology, University of Antwerp, 2610 Wilrijk, Belgium*; orcid.org/0000-0001-5334-7655

Complete contact information is available at: https://pubs.acs.org/10.1021/acs.analchem.1c00298

Author Contributions

The manuscript was written through contributions of all authors. All authors have given approval to the final version of the manuscript

Notes

The authors declare no competing financial interest.

ACKNOWLEDGMENTS

The authors acknowledge Bart Cleuren and Robin Bonné from UHasselt for the discussion on the C-AFM experiment. The authors acknowledge the grants given by the Research Foundation − Flanders (FWO) (G031416N to R.T.E., J.V.M., and F.J.R.M.; G038819N to F.J.R.M.) and the Netherlands Organization for Scientific Research (NWO) (VICI grant 016.VICI.170.072 awarded to F.J.R.M.). ToF-SIMS analysis was rendered possible, thanks to the grant awarded to imec vzw and Hasselt University by the Hercules foundation (now FWO; grant no. ZW/13/07 awarded to J.V.M. and A.F.).

REFERENCES

(1) Pfeffer, C.; Larsen, S.; Song, J.; Dong, M.; Besenbacher, F.; Meyer, R. L.; Kjeldsen, K. U.; Schreiber, L.; Gorby, Y. A.; El-Naggar, M. Y.; Leung, K. M.; Schramm, A.; Risgaard-Petersen, N.; Nielsen, L. P. *Nature* **2012**, *491*, 218−221.

(2) Schauer, R.; Risgaard-Petersen, N.; Kjeldsen, K. U.; Bjerg, J. J. T.; Jorgensen, B. B.; Schramm, A.; Nielsen, L. P. *ISME J.* **2014**, *8*, 1314−1322.

(3) Meysman, F. J. R. *Trends Microbiol.* **2018**, *26*, 411−422.

(4) Risgaard-Petersen, N.; Kristiansen, M.; Frederiksen, R. B.; Dittmer, A. L.; Bjerg, J. T.; Trojan, D.; Schreiber, L.; Damgaard, L. R.; Schramm, A.; Nielsen, L. P. *Appl. Environ. Microbiol.* **2015**, *81*, 6003−6011.

(5) Müller, H.; Bosch, J.; Griebler, C.; Damgaard, L. R.; Nielsen, L. P.; Lueders, T.; Meckenstock, R. U. *ISME J.* **2016**, *10*, 2010−2019.

(6) Malkin, S. Y.; Rao, A. M.; Seitaj, D.; Vasquez-Cardenas, D.; Zetsche, E.-M.; Hidalgo-Martinez, S.; Boschker, H. T.; Meysman, F. J. *ISME J.* **2014**, *8*, 1843−1854.

(7) Burdorf, L. D. W.; Tramper, A.; Seitaj, D.; Meire, L.; Hidalgo-Martinez, S.; Zetsche, E. M.; Boschker, H. T. S.; Meysman, F. J. R. *Biogeosciences* **2017**, *14*, 683−701.

(8) Cornelissen, R.; Bøggild, A.; Thiruvallur Eachambadi, R.; Koning, R. I.; Kremer, A.; Hidalgo-Martinez, S.; Zetsche, E.-M.; Damgaard, L. R.; Bonné, R.; Drijkoningen, J.; Geelhoed, J. S.; Boesen, T.; Boschker, H. T. S.; Valcke, R.; Nielsen, L. P.; D'Haen, J.; Manca, J. V.; Meysman, F. J. R. *Front. Microbiol.* **2018**, *9*, No. 3044.

(9) Meysman, F. J. R.; Cornelissen, R.; Trashin, S.; Bonné, R.; Martinez, S. H.; van der Veen, J.; Blom, C. J.; Karman, C.; Hou, J. L.; Eachambadi, R. T.; Geelhoed, J. S.; Wael, K.; Beaumont, H. J. E.; Cleuren, B.; Valcke, R.; van der Zant, H. S. J.; Boschker, H. T. S.; Manca, J. V. *Nat. Commun.* **2019**, *10*, No. 4120.

(10) Thiruvallur Eachambadi, R.; Bonné, R.; Cornelissen, R.; Hidalgo-Martinez, S.; Vangronsveld, J.; Meysman, F. J. R.; Valcke, R.; Cleuren, B.; Manca, J. V. *Adv. Biosyst.* **2020**, *4*, No. 2000006.

(11) Boschker, H. T. S.; Cook, P. L.; Polerecky, L.; Thiruvallur Eachambadi, R.; Lozano, H.; Hidalgo-Martinez, S.; Khalenkow, D.; Spampinato, V.; Claes, N.; Kundu, P.; Wang, D.; Bals, S.; Cavezza, F.; Hauffman, T.; Tataru Bjerg, J.; Skirtach, A. G.; Kochan, K.; McKee, M.; Wood, B.; Bedolla, D.; Geerlings, N. M.; Van Gerven, N.; Remaut, H.; Millan-Solsona, R.; Fumagalli, L.; Nielsen, L.-P.; Franquet, A.; Manca, J. V.; Gomila, G.; Meysman, F. J. R. *bioRxiv* **2020**, No. 10.23.351973.

(12) Hanrieder, J.; Malmberg, P.; Ewing, A. G. *Biochim. Biophys. Acta, Proteins Proteomics* **2015**, *1854*, 718−731.

(13) Jungnickel, H.; Laux, P.; Luch, A. *Toxics* **2016**, *4*, 5.

(14) Spengler, B. *Anal. Chem.* **2015**, *87*, 64−82.

(15) Smart, K. E.; Smith, J. A. C.; Kilburn, M. R.; Martin, B. G. H.; Hawes, C.; Grovenor, C. R. M. *Plant J.* **2010**, *63*, 870−879.

(16) Malherbe, J.; Penen, F.; Isaure, M. P.; Frank, J.; Hause, G.; Dobritzsch, D.; Gontier, E.; Horréard, F.; Hillion, F.; Schaumlöffel, D. *Anal. Chem.* **2016**, *88*, 7130−7136.

(17) Agüi-Gonzalez, P.; Jähne, S.; Phan, N. T. N. *J. Anal. At. Spectrom.* **2019**, *34*, 1355−1368.

(18) Nuñez, J.; Renslow, R.; Cliff, J. B.; Anderton, C. R. *Biointerphases* **2018**, *13*, No. 03B301.

(19) Gyngard, F.; Steinhauser, M. L. *J. Anal. At. Spectrom.* **2019**, *34*, 1534−1545.

(20) Georgantzopoulou, A.; Serchi, T.; Cambier, S.; Leclercq, C. C.; Renaut, J.; Shao, J.; Kruszewski, M.; Lentzen, E.; Grysan, P.; Eswara, S.; Audinot, J. N.; Contal, S.; Ziebel, J.; Guignard, C.; Hoffmann, L.; Murk, A. T. J.; Gutleb, A. C. *Part. Fibre Toxicol.* **2015**, *13*, No. 9.

(21) Lee, R. F. S.; Riedel, T.; Escrig, S.; Maclachlan, C.; Knott, G. W.; Davey, C. A.; Johnsson, K.; Meibom, A.; Dyson, P. J. *Metallomics* **2017**, *9*, 1413−1420.

(22) Geerlings, N. M. J.; Karman, C.; Trashin, S.; As, K. S.; Kienhuis, M. V. M.; Hidalgo-Martinez, S.; Vasquez-Cardenas, D.; Boschker, H. T. S.; de Wael, K.; Middelburg, J. J.; Polerecky, L.; Meysman, F. J. R. *Proc. Natl. Acad. Sci. U.S.A.* **2020**, *117*, 5478−5485.

(23) Dubey, M.; Brison, J.; Grainger, D. W.; Castner, D. G. *Surf. Interface Anal.* **2011**, *43*, 261−264.
(24) Decelle, J.; Veronesi, G.; Gallet, B.; Stryhanyuk, H.; Benettoni, P.; Schmidt, M.; Tucoulou, R.; Passarelli, M.; Bohic, S.; Clode, P.; Musat, N. *Trends Cell Biol.* **2020**, *30*, 173−188.
(25) Vanbellingen, Q. P.; Elie, N.; Eller, M. J.; Della-Negra, S.; Touboul, D.; Brunelle, A. *Rapid Commun. Mass Spectrom.* **2015**, *29*, 1187−1195.
(26) Kubicek, M.; Holzlechner, G.; Opitz, A. K.; Larisegger, S.; Hutter, H.; Fleig, J. *Appl. Surf. Sci.* **2014**, *289*, 407−416.
(27) Henss, A.; Otto, S.-K.; Schaepe, K.; Pauksch, L.; Lips, K. S.; Rohnke, M. *Biointerphases* **2018**, *13*, No. 03B410.
(28) Benettoni, P.; Stryhanyuk, H.; Wagner, S.; Kollmer, F.; Moreno Osorio, J. H.; Schmidt, M.; Reemtsma, T.; Richnow, H. H. *J. Anal. At. Spectrom.* **2019**, *34*, 1098−1108.
(29) Jiang, Z.; Zhang, S.; Klausen, L. H.; Song, J.; Li, Q.; Wang, Z.; Stokke, B. T.; Huang, Y.; Besenbacher, F.; Nielsen, L. P.; Dong, M. *Proc. Natl. Acad. Sci. U.S.A.* **2018**, *115*, 8517−8522.
(30) Bonné, R.; Hou, J. L.; Hustings, J.; Wouters, K.; Meert, M.; Hidalgo-Martinez, S.; Cornelissen, R.; Morini, F.; Thijs, S.; Vangronsveld, J.; Valcke, R.; Cleuren, B.; Meysman, F. J. R.; Manca, J. V. *Sci. Rep.* **2020**, *10*, No. 19798.

https://doi.org/10.1021/acs.analchem.1c00298
Anal. Chem. 2021, 93, 7226−7234